Large-scale Magnetic Field Oscillations and Their Effects on **Modulating Energetic Electron Precipitation**

Murong Qin¹, Wen Li¹, Qianli Ma^{1,2}, Xiao-Chen Shen¹, Leslie Woodger³, Robyn Millan³ and 1 Vassilis Angelopoulos⁴ 2

- 3 ¹ Center for Space Physics, Boston University, Boston, Massachusetts, USA
- ² Department of Atmospheric and Oceanic Sciences, University of California, Los Angeles, 4
- California, USA 5
- ³ Department of Physics and Astronomy, Dartmouth College, Hanover, New Hampshire, USA 6
- ⁴ Earth, Planetary, and Space Sciences Department, University of California, Los Angeles, 7
- California, USA 8

- 10 * Correspondence:
- Murong Qin 11
- 12 mgin1@bu.edu
- 13 Wen Li
- 14 wenli77@bu.edu
- 15 Keywords: wave-particle interaction₁, magnetic field oscillations₂, ULF waves₃, whistler
- 16 waves₄, electron precipitation₅.
- 17 **Abstract**
- 18 In this study, we present simultaneous multi-point observations of magnetospheric oscillations on a
- time scale of several to tens of minutes and modulated whistler-mode chorus waves, associated with 19
- concurrent energetic electron precipitation observed through enhanced BARREL X-rays. Similar 20
- fluctuations are observed in X-ray signatures and the compressional component of magnetic 21
- oscillations, spanning from ~9 to 12 h in MLT and 5 to 11 in L shell. Such magnetospheric oscillations 22
- covering an extensive region in the pre-noon sector have been suggested to play a potential role in 23
- 24 precipitating energetic electrons by either wave scattering or loss cone modulation, showing a high
- correlation with the enhancement in X-rays. In this event, the correlation coefficients between chorus 25
- waves (smoothed over 8 min), ambient magnetic field oscillations and X-rays are high. We perform an 26
- in-depth quasi-linear modeling analysis to evaluate the role of magnetic field oscillations in modulating 27
- 28 energetic electron precipitation in the Earth's magnetosphere through modulating whistler-mode
- 29 chorus wave amplitude, resonance condition between chorus waves and electrons, as well as loss cone
- 30 size. Model results further show that the modulation of chorus wave amplitude plays a dominant role
- in modulating the electron precipitation. However, the effect of the modulation in the resonant energy 31
- between chorus waves and energetic electrons due to the background magnetic field oscillations cannot 32
- be neglected. The bounce loss cone modulation, affected by the magnetic oscillations, has little 33
- influence on the electron precipitation modulation. Our results show that the low frequency 34
- magnetospheric oscillations could play a significant role in modulating the electron precipitation 35
- through modulating chorus wave intensity and the resonant energy between chorus waves and electron. 36

1 Introduction

- 38 Pitch angle diffusion of energetic electrons into the atmospheric bounce loss cone has been considered
- 39 to be an important loss mechanism of radiation belt electrons. In this process, energetic electrons are
- 40 precipitated into the atmosphere through resonant interactions with various plasma waves (e.g., Millan
- and Thorne., 2007), such as electromagnetic ion cyclotron (EMIC) waves (Summers et al., 2003; 41
- 42 Capannolo et al., 2019a, 2019b; Clilverd et al., 2015; Hendry et al., 2017; Oin et al., 2018, 2019, 2020;
- Zhang et al., 2021), whistler-mode chorus waves (e.g., Thorne et al., 2010; Nishimura et al., 2010; Ma 43
- et al., 2020) and hiss waves in the plasmasphere and plumes (Summers et al., 2008; Li et al., 2019; Ma 44
- 45 et al., 2021).

- 46 Fluctuations with frequencies below tens of millihertz (mHz) have been extensively observed in the
- 47 signatures of energetic electron precipitation from riometer pulsations (*Heacock & Hunsucker*, 1977;
- Spanswick et al., 2005), radars (Buchert et al., 1999), optical auroral emissions (Jaynes et al., 2015; 48
- 49 Rae et al., 2007) and balloon X-ray spectra (Brito et al., 2012; Halford et al., 2015; Motoba et al.,
- 2013; Breneman et al., 2015, 2020; Rae et al., 2018; Qin et al., 2021). These fluctuations have been 50
- 51 shown to be usually associated with ultra-low frequency (ULF) waves or quasi-static breathing mode
- 52 of the magnetosphere with similar periodicities. Pc 3–5 ULF waves (4–22 mHz) can be driven by
- 53 upstream solar wind dynamic pressure impulses (e.g., Claudepierre et al., 2009; Claudepierre et al.,
- 54 2010; Shen et al., 2015, 2017), solar wind speed changes (Mathie & Mann, 2001), as well as internal
- sources like substorms (e.g., Hsu & McPherron, 2007; Olson, 1999). The magnetosphere also responds 55
- 56 to external solar wind conditions via a quasi-static forced breathing mode, with periods longer than the
- 57 Alfven wave travel time in the dayside magnetosphere (~4 min, 4 mHz) (Kepko et al., 2002; Kepko &
- Spence, 2003; Kepko & Viall, 2019). Because the period of these ambient magnetic field oscillations 58
- 59 is much longer than the gyroperiod and the bounce period of energetic electrons, they are only supposed
- 60 to be in drift resonance with electrons (Elkington et al., 2003), rather than directly scatter the electrons
- 61 into loss cone through cyclotron-resonance interaction.
- 62 Many mechanisms have been employed to explain the commonly observed energetic electron
- precipitation modulated by ULF wave or quasi-static breathing mode oscillations. Theoretically, ULF 63
- waves or quasi-static breathing mode magnetic field fluctuations can modulate electron precipitation 64
- mainly in three ways. (1) ULF waves/breathing mode oscillations can modulate the EMIC wave and 65
- 66 whistler-mode wave growth rate. Breneman et al. (2015) showed that 1-10 min ULF modulations of
- X-rays generated by electron precipitation on a Balloon Array for Radiation-belt Relativistic Electron 67
- Losses (BARREL) balloon (Millan et al., 2013; Woodger et al., 2015) were nearly identical to 68
- modulations in whistler-mode hiss amplitude observed by the Van Allen Probes (RBSP, Mauk et al., 69
- 70 2013) during a close magnetic conjunction. Breneman et al. (2020) reported large-scale electron
- precipitation observed as X-rays on BARREL. Their analysis suggested that hiss waves modulated by 71
- 72 forced-breathing mode magnetic field fluctuations are directly responsible for the observed loss. (2)
- 73 ULF waves/breathing mode oscillations could modulate the resonance condition and thus cause an
- 74 increase/decrease of the resonant energy with electrons by modulating the ambient magnetic field or
- 75 total electron density. Zhang et al. (2019) investigated the mechanism of electron precipitation through
- quasi-linear pitch angle scattering by EMIC waves when simultaneous ULF waves exist. It was shown
- 76
- that the ULF wave fluctuations could lead to a significant decrease in the minimum resonant energy 77
- when the magnetic field diminishes. (3) ULF waves can cause electron precipitation by modulating the 78
- 79 size of the bounce loss cone (BLC) (Rae et al., 2018) and electron pitch angles (Brito et al., 2012; 2015;
- Yin et al., 2023). Brito et al. (2012, 2015) used MHD simulations to show that when electrons encounter 80
- compressional magnetic field oscillations, their trajectories move closer to the Earth into a stronger 81
- 82 magnetic field with shorter field lines where the loss cone is larger, leading to enhanced precipitation.
- 83 However, due to a lack of equatorial wave observations and direct comparison between observed and

simulated electron precipitation features, it remains unclear whether ULF waves were fully responsible for the electron precipitation or act as a minor role in modulating electron precipitation. ULF waves/breathing mode oscillations could also modulate the BLC by modulating the ambient magnetic field (Rae et al., 2018). Although the direct modulation of the BLC by ULF waves/quasi-static breathing mode only influences electrons near the loss cone, it could potentially enhance the modulation of precipitation during the presence of EMIC/whistler-mode waves due to pitch angle scattering. However, there are no means to test other precipitation sources, such as pitch angle scattering by whistler-mode waves, due to the lack of conjugated high frequency wave measurement near the equatorial plane.

In this paper, we primarily use observations from BARREL-1H (*Millan et al.*, 2013) and THEMIS-E (*Angelopoulos*, 2008), which were in close conjunction, to separately evaluate the effect of whistler-mode chorus wave amplitude, loss cone size and the resonant energy (between plasma waves and electrons) in modulating energetic electron precipitation in the Earth's magnetosphere. We also augment our observations with other equatorial satellite magnetometer data from THEMIS-D, RBSP-A, B and GOES-13, 15 (*Singer et al.*, 1996), as well as the observations of X-rays generated by electron precipitation from other BARREL payloads (BARREL 1A, 1I, 1Q, 1T and 1U). The BARREL payloads drift slowly in space, enabling the investigation of temporal evolution features of electron precipitation. The THEMIS spacecraft were operating in near-equatorial orbits to measure waves and plasma parameters.

The content of the paper is outlined as follows. In section 2, an overview of the event and detailed correlation between the measured chorus emissions, BARREL X-rays and quasi-static breathing mode fluctuations are presented. In section 3, through a physics-based technique based on the quasi-linear theory, we quantify the role of background magnetic field in modulating the chorus-driven electron precipitation by turning on and off the background quasi-static magnetic field fluctuations respectively and compare the time evolution of the modeled electron precipitation with the observed modulated X-rays. In section 4, we discuss the potential roles of loss cone change and the shift of resonant energy in modulating the energetic electron precipitation. The conclusions are summarized in section 5.

2 Observation

2.1 Event overview

Figure 1a shows the trajectories of the available equatorial satellites (THEMIS-D, E; RBSP-B and GOES-13, 15) and BARREL payloads (BARREL 1A, 1H, 1I, 1Q, 1T and 1U) in the L-MLT map (determined using the IGRF magnetic field model) over 18:30 UT – 20:30 UT on 28 January 2013. Figures 1 (b-d) show solar wind and geomagnetic conditions, indicating little change in the interplanetary magnetic field and the solar wind dynamic pressure, as well as a modest substorm activity at around 18:30 UT. Figures 1f and 1g show the fluxgate magnetometer data from GOES and THEMIS. During this event, GOES-15 and GOES-13 were located in the pre-noon and post-noon sectors respectively (Figure 1a), providing observations of magnetic field at geosynchronous orbit with 0.512 s time resolution. THEMIS-D and THEMIS-E were located in the pre-noon sector outside the geosynchronous orbit. Following the substorm onset (18:30 UT), similar magnetic field modulations (correlation coefficient > 0.5) on a timescale of ~10s of minutes (forced-breathing mode) were observed by GOES-15, THEMIS-D, and THEMIS-E. Such low frequency magnetospheric oscillations are often related to solar wind pressure variations (Kepko et al., 2002; Kepko & Spence, 2003). In this event, however, no corresponding oscillations were observed in the solar wind data (OMNI database, propagated from measurements at the Lagrange-1 point by either ACE or Wind satellite to the Earth's bow shock nose). ARTEMIS satellites, which can also be used to monitor the solar wind conditions 130 (Artemyev et al., 2018), were located at \sim 60 $R_{\rm E}$ in the magnetotail instead of in the dayside solar wind,

and thus unable to provide the solar wind data. The driver of such low frequency magnetospheric

oscillations is still unclear. GOES-13, which was located near post-noon, however, shows a different

modulation in the background magnetic field (Figure 1f).

148

149

150

151

152

153

154

155

156

157

158

159

160

161

162163

164

165166

167

168 169

170

171

172

173

174

175

134 Observations from the full BARREL array are shown in the 25-180 keV X-ray fast spectrum smoothed 135 over 0.5s (Millan et al., 2013; Woodger et al., 2015) in Figure 1h. Similar modulations were observed 136 on BARREL 1H and 1Q, which were located in the prenoon sector. The count rate level of X-rays was 137 higher for BARREL 1H ($L \sim 8$) than 1Q ($L \sim 5$), which might be either caused by the different trapped 138 flux levels at different L shells or the location of the plasmapause. Enhancements were not observed 139 on BARREL-1A, 1I, 1T and 1U, which were located in the afternoon sector. Those satellites and 140 payloads with similar fluctuations (correlation coefficient > 0.5) are highlighted in the black boxes in 141 Figure 1a. The spatial scale with the similar modulation timescale is large, with MLT spanning from 142 ~9 to 12 and L shell from 5 to 11. It was also shown that moderate changes in the ambient magnetic 143 field can cause a significant change in the BLC (Rae et al., 2018), the plasma wave growth rate and the resonance condition between waves and energetic electrons (Zhang et al., 2019). In this case, the 144 145 relative change (relative to the 60 min smoothed data) of the magnetic field on THEMIS-D and E 146 reached up to around 10% (Figure 1i). Our results indicate a potential link between the low frequency magnetic field fluctuations and the electron precipitation observed through BARREL X-rays. 147

To explore the modulation in electron precipitation, background magnetic field fluctuations, and whistler-mode chorus waves, we analyze the observations from BARREL-1H and THEMIS-E which were in closer conjunction (Figure 2). Figure 2a shows three components of the magnetic field in the field-aligned coordinates observed by THEMIS-E flux gate magnetometers (FGM) (Auster et al., 2008), which were detrended over 60 min to show the ULF/quasi-static forced breathing mode variations. It is shown that the compressional component (red line) has a similar fluctuation to the BARREL X-rays shown in Figure 2e. Figure 2b shows the magnetic spectral density observed by the Search Coil Magnetometer (SCM) (Roux et al., 2008), which detects low-frequency magnetic field fluctuations and waves in three directions over a frequency bandwidth up to ~8 kHz. The superimposed magenta line represents total electron density inferred from the spacecraft potential (Pedersen et al., 2008) measured by the Electric Field Instrument (EFI) (Bonnell et al., 2008). The lower-band chorus wave was also observed by THEMIS-E and the wave intensity was positively correlated with the total electron density, with the lower cutoff frequency of waves extending down to a lower value with a higher density. The density modulation can lead to modulation of chorus wave growth through modulating the fraction of resonant electrons (W. Li et al., 2011) or through wave trapping by density crests or troughs (Chen et al., 2012; Liu et al., 2021). Figure 2c shows the magnetic spectral density calculated from the low frequency fluctuations (up to 64 Hz) of the background magnetic field measured by the FGM instrument, using fast Fourier transform method with a window size of 256 s and a shifted time window by 32 s. EMIC waves were also detected during this event. However, the enhancement in X-rays were only observed in the lowest energy channel (25–180 keV). EMIC waves, which are known to interact with high-energy electrons (>~ a few hundred keV: Capannolo et al., 2019a, 2019b: Grach et al., 2022) and would lead to enhanced X-ray count rates in higher energy channels (Z. Li et al., 2014), are unlikely to play a major role during this precipitation event. Figure 2d shows the Morlet mother wavelet analysis of the FGM measurement. The horizontal lines in panel (d) indicate frequencies of 4 mHz and 30 mHz. ULF waves between 4 mHz and 30 mHz were relatively weak, while the quasi-static forced breathing mode, with wave frequency lower than 4 mHz, was stronger. The forced breathing mode of the magnetosphere was associated with the enhancement of the 25-180 keV BARREL X-rays with a similar fluctuation, as shown in Figure 2e.

2.2 Modulation of waves and electron precipitation

176

177

178179

180 181

182 183

184

185

186 187

188

189

190

191

192

193

194

195

196

197

198 199

200

201202

203

204

205

206

207

208209

210

211212

213

214

215216

217

218219

220

221222

In order to examine the correlation between the observed electron precipitation and the chorus waves or ambient magnetic field oscillations, we show the correlation coefficients (C. C.) between them in Figure 3. During this period, chorus waves were observed outside the plasmasphere, as shown in Figure 2b. The blue line in Figure 3a shows chorus wave amplitude (8-s time resolution, blue line) observed by THEMIS-E, which was calculated by integrating the wave intensity over the frequency range from 100 Hz to 1000 Hz. The black line in Figure 3a shows the total electron density inferred from the spacecraft potential. It shows that the chorus wave intensity has similar fluctuations with the local electron density on a timescale of approximately one minute. However, when considering a longer time scale (10s of minutes), the fluctuations of chorus waves and electron density are quite different. This is evident in the correlation coefficient over the entire time window (19:10-20:30), which is only 0.02 (Figure 3a). To analyze the correlation on a shorter timescale, Figure 3f presents the calculation of the correlation coefficient within a 4-min box with a time-shifted window of 2 minutes. Figure 3f shows that the chorus wave intensity is highly correlated (>0.5 at most times) with the local electron density, further supporting that the chorus waves are modulated by local density. Figure 3b shows the amplitudes of chorus waves (blue line) and the compressional component of the ambient magnetic field oscillations (0.6–30 mHz, 4-s time resolution, black line), with a low correlation coefficient only about 0.15. Figure 3c shows the X-ray count rate (black line) and the chorus wave amplitude (blue line), also with a low correlation of about 0.22. Similarly, we calculate the short-time scale correlation, which is shown in Figure 3e and further demonstrates the overall low correlation (C. C. < 0.5 at most times). Figure 3d shows the compressional component of the ambient magnetic field oscillations (black line) and the X-ray count rate (magenta line), with a correlation coefficient ~ 0.62, much higher than that between X-ray count rate and chorus wave amplitude. This indicates that the breathing mode fluctuations observed by THEMIS-E is highly correlated with the enhancement in X-rays. Combining with the fact that a similar modulation (C. C. > 0.5) was also observed by BARREL-1Q and GOES-15 (Figure 1a), we conclude that the quasi-static breathing mode may have played a significant role in modulating the electron precipitation. Previous studies show high correlation between chorus waves and ASI auroral intensity when the electron precipitation is driven by chorus waves (Nishimura et al., 2011; Hosokawa et al., 2020). In those work, the observations were specifically chosen at latitudes with the highest correlation (corresponding to highest correlation L shell), within a narrow window of a few minutes. In this case, however, the correlation is calculated on a point-to-point basis, rather than the point-to-plane comparison in (Nishimura et al., 2011; Hosokawa et al., 2020). The low correlation between chorus wave amplitude and X-ray count rate (Figure 3e) might be due to the spatial difference of THEMIS-E and BARREL-1H, which were at rough conjugate locations with a separation in L shell of ~1.5-2.5. This is much larger than the coherent scale size of the chorus elements, which is about hundreds to thousands of kilometers (Agapitov et al., 2017; Shen et al., 2019), thus the electron precipitation is not expected to have one-to-one correspondence with the chorus wave elements.

The chorus wave intensity is not only shown to be correlated (at times) with the local electron density (Figure 3f), but also tends to increase (decrease) when the ambient background magnetic field increases (decreases). The ambient magnetic field oscillations can modulate the whistler mode growth rate by modulating the magnetic field inhomogeneity (Zhou et al., 2015) and the radial transport of resonant electron populations (*Brenaman et al.*, 2020). To smooth out the modulation in association with local plasma density, whistler-mode chorus wave amplitude is smoothed over 8 min to evaluate the temporal modulation on forced-breathing time scale. The results are shown in Figure 4, which is similar to Figure 3 except that chorus wave amplitude is smoothed over 8 min. The analysis reveals that there is a notable increase in the correlation coefficient between chorus wave intensity (smoothed over 8-min) and the amplitude of the ambient magnetic field fluctuations (Figure 4a), reaching 0.39. This value is higher

when compared to the correlation coefficient of 0.15 for unsmoothed chorus wave amplitude in Figure 3b. Additionally, the correlation coefficient between the smoothed chorus wave amplitude and X-ray count rate (Figure 4b) increased to 0.62. This value is much higher compared to the unsmoothed case in Figure 3c (C. C. ~ 0.22) and comparable to the correlation coefficient between the ambient magnetic field fluctuations and X-ray count rate (Figure 4c). These findings suggest that the overall temporal evolution of chorus wave amplitude is also modulated by quasi-static breathing mode oscillations of the ambient magnetic field, which can further modulate the X-ray count rate generated by electron precipitation. Since the magnetic field oscillations can also modulate electron precipitation through modulating resonance condition and the loss cone size, the correlation analysis itself cannot determine the main driver of the electron precipitation modulation. To further examine the role of each mechanism, a further physics-based modeling is performed in Section 3 and Section 4.

3 Comparison between observations and simulations

Figure 5a shows the modulation in equatorial bounce loss cone (blue) due to large amplitude magnetic field oscillations (black). The equatorial bounce loss cone α_{LC} is defined as the maximum pitch angle of particles at the equatorial plane that have a mirror point below 100 km altitude in the atmosphere $(sin^2\alpha_{LC}=B_0/B_m)$, where B_0 is the equatorial magnetic field and B_m is the magnetic field at 100 km altitude). Since the variation in B_m is only a small fraction of B_m as compared to B_0 , we assume that the variation in α_{LC} is mainly caused by modulation in B_0 with very little loss in accuracy (*Rae et al.*, 2018). Magnetic field strength of B_m was calculated by mapping the THEMIS-E position to the foot point at 100 km using the IGRF magnetic field model. The ratio of the corresponding background magnetic field and loss cone size under the two circumstances are shown in Figure 5g, where the black line represents magnetic field and the blue line is for the equatorial loss cone size. When B_0 increases, the equatorial loss cone size also increases, which allows more particles to be precipitated. It is shown that there is an up to 8% variation in loss cone size caused by ambient magnetic field fluctuations.

The pitch angle scattering rates driven by chorus waves are quantified using a physics-based approach with the Full Diffusion Code to calculate the quasi-linear diffusion coefficients ($Ni\ et\ al.$, 2008). Landau resonance and multiple cyclotron harmonic resonances (-10 to 10) are considered. It is assumed that chorus wave normal angles are quasi-parallel to the magnetic field line near the equatorial plane and increase as magnetic latitudes increase ($Ni\ et\ al.$, 2013). Total electron density is derived from the spacecraft potential measured by THEMIS-E and assumed to be constant along the field lines. With the diffusion coefficient $< D_{\alpha\alpha}>_{LC}$ and the electron flux near the equatorial loss cone α_{LC} , we then determine the equatorial pitch angle distribution of electrons inside the loss cone using the solution for the Fokker-Planck equation under the quasi-equilibrium state ($Kennel\ \&\ Petschek$, 1966; W. $Li\ et\ al.$, 2013; $Ma\ et\ al.$, 2020, 2021), which can be estimated as:

$$J_{in}(\alpha_{eq,in}, E) = \frac{S(E)}{D^*} \left\{ \frac{I_0(\frac{\alpha_{eq,in}}{\alpha_{LC}} z_0)}{z_0 I_1(z_0)} \right\}$$
 (1)

where I_0 and I_1 are the modified Bessel functions; S(E) is the rate that the particles enter the loss cone, which is calculated based on the electron flux measured by solid state telescope (SST) onboard THEMIS-E at the lowest pitch angle bin (11.25°); $D^* \approx < D_{aa} >_{LC} \times cos \ (\alpha_{LC})$ and $Z_0 = \frac{\alpha_{LC}}{\sqrt{D^*\tau}}$, where τ is a quarter of the electron bounce period. The integral electron flux inside the loss cone is further calculated as:

$$J_{integral}(E) = \int_{0}^{\alpha_{LC}} J_{in}(\alpha_{eq,in}, E) \cdot \sin\alpha \cdot d\alpha$$
 (2)

264 In order to evaluate the effects of ambient magnetic field oscillations in electron precipitation through 265 modulating the resonance condition and loss cone size, we perform simulations by turning on ("modulated") and turning off ("smoothed") the background ambient magnetic field fluctuations in the 266 267 Full Diffusion Code and in calculating the resultant integral electron precipitation inside the loss cone using Equations (1) and (2). In the "modulated" case, the modulation of chorus wave amplitude and 268 269 modulation of the resonant energy are included to calculate the diffusion coefficients with the Full 270 Diffusion Code (Figure 5b) and the modulation of the loss cone size is further included to calculate the 271 resultant electron precipitation using Equations (1) and (2) (Figure 5c). In the "smoothed" case, only the modulation of the chorus wave amplitude is included to calculate the diffusion coefficients (Figure 272 273 5e) and the electron precipitation (Figure 5f). The ratios of them are shown in the right panels (g-i).

274 The diffusion coefficients at the loss cone $\langle D_{\alpha\alpha} \rangle_{LC}$ corresponding to these two circumstances are shown in Figure 5b (Modulated) and 5e (Smoothed). The superimposed black lines are BARREL X-276 ray counts at 25-180 keV. Figure 5h is the ratio between them. When background magnetic field increases, chorus waves tend to interact with higher energy electrons more efficiently, leading to a 278 higher ratio in $< D_{\alpha\alpha} >_{LC}$ (modulated/smoothed) at higher energies and a lower ratio at lower energies. Above 30 keV, breathing mode can decrease the diffusion coefficient to half at minimum B_0 and 279 increase the diffusion coefficient by 50% at maximum B_0 . The modulations of $\langle D_{\alpha\alpha} \rangle_{LC}$ caused by 280 chorus wave amplitude variations are more noticeable than the difference of $< D_{\alpha\alpha} >_{LC}$ caused by the 282 modulation of resonant condition (mainly due to the modulation of background magnetic field), as shown in Figures 5b and 5e. This indicates that the temporal modulation of the chorus wave amplitude 284 dominates the fluctuations in electron precipitation.

285 Figures 5c and 5f show the integral precipitating flux under the two circumstances and Figure 5i is the 286 ratio between them. It was shown that the integral precipitating flux is similar for the two circumstances 287 when the background magnetic field fluctuation is turned on (Figure 5c) and turned off (Figure 5f). 288 The ratio in Figure 5i further shows that the precipitating fluxes at higher energy (>~100 keV) are 289 significantly modulated. The modeled precipitation can increase by 1.5-3 times as magnetic field varies 290 from the minimum to maximum value when we turn on the breathing mode fluctuation. This result 291 indicates that although the temporal modulation of the chorus wave amplitude dominates the 292 fluctuations in electron precipitation, the effects of the modulation of resonance condition through 293 modulating the background magnetic field cannot be neglected.

4 **Discussion**

275

277

281

283

- 295 In this work, we evaluate the role of breathing mode magnetic field oscillations in modulating the 296 electron precipitation. Although the ambient magnetic field oscillations alone only affect the small 297 electron population near the loss cone, they can play an important role in modulating the electron 298 precipitation ratio with the presence of chorus waves, through modulating the chorus wave amplitude, 299 the resonance condition and the loss cone size.
- 300 ULF waves/forced-breathing mode magnetic field fluctuations can modulate the electron precipitation 301 through modulating chorus wave growth rate (e.g., Breneman et al., 2015; Jaynes et al., 2015; W. Li et 302 al., 2011a; Qin et al., 2021; Xia et al., 2016). In our study, the whistler-mode chorus wave amplitude 303 is modulated by both magnetic field fluctuations (Figure 4a) and local electron density (Figure 3f). The 304 correlation coefficient between chorus wave amplitude (8 s time resolution without smoothing) and the electron precipitation is low (0.22). This is because the separation in L shell between chorus wave and 305 306 electron precipitation is ~1.5-2.5, much larger than the coherent scale size of the chorus elements, 307 which is about hundreds to thousands of kilometers (Agapitov et al., 2017; Shen et al., 2019). Therefore, 308 the electron precipitation is not expected to have one-to-one correspondence with the chorus wave

309 elements. The smoothed chorus wave amplitude, which shows the averaged properties of a group of 310 chorus wave elements, however, exhibits a higher correlation (0.62) with X-ray count rate (Figure 4b). 311 This suggests that the magnetic field oscillations could modulate the electron precipitation through 312 modulating the whistler-mode chorus wave amplitude. The maximum value of the smoothed chorus 313 wave amplitude is about 4 times larger than the minimum value, which can lead to a significant 314 modulation (16 times) in the electron precipitation. Unfortunately, chorus wave intensity measured at 315 the exactly same location as BARREL was not available, and thus the accurate role of the modulation 316 of chorus wave intensity in modulating the energetic electron precipitation is difficult to quantify.

317

318

319

320

321

322

323

324

325

326

327

328 329

330

331

332333

334

335

336

337338

339

340

341

342

343

344

345

346

347348

349

350

351

352

353354355

ULF waves/forced-breathing mode magnetic field fluctuations can also modulate the electron precipitation through modulating the resonance condition and the loss cone size. On one hand, the minimum energy of electrons to interact with chorus waves depends on the background magnetic field strength. Zhang et al. (2019) investigated the mechanism of electron precipitation through quasi-linear pitch angle scattering by EMIC waves when ULF waves coexist. It was shown that the ULF wave fluctuation could lead to a decrease in the minimum resonant energy when the magnetic field diminishes. On the other hand, chorus waves can move electrons toward pitch angles near the loss cone through cyclotron resonance. The quasi-static breathing mode magnetic field oscillations can then take over and enhance (reduce) the precipitation by increasing (decreasing) the loss cone size, as suggested by Rae et al., (2018). In our case, we show that magnetic field fluctuations could affect the resonant energy and the pitch angle diffusion rate (Figure 5). When the magnetic field increases (decreases), the minimum energy for electrons to be in resonance with chorus waves increases (decreases, approximately ~10%). For electrons above 30 keV, the diffusion coefficients at the loss cone increase by up to ~1.5 times when the magnetic field increases by 5%. Correspondingly, the diffusion coefficients for electrons with energy below 30 keV show an anti-correlation with the magnetic field oscillations. Since BARREL X-rays are only sensitive to electrons with energy approximately above 30 keV, the X-ray count rate is expected to increase when the background magnetic field increases.

In order to separate the effect of bounce loss cone size modulation and the effect of diffusion coefficient modulation on the precipitating flux, we further compare the simulation results corresponding to three cases: (1) in the "smoothed" case, only the modulation of the chorus wave amplitude is included to calculate the diffusion coefficient and electron precipitation; (2) in the case of "modulated loss cone", the modulation of the chorus wave amplitude is included to calculate the diffusion coefficient and the modulation of loss cone is further included to calculate the electron precipitation (the modulation of resonant energy is not included to calculate the diffusion coefficient and the resultant integral electron precipitation inside the loss cone); (3) in the case of "modulated diffusion coefficient", both modulation of the chorus wave amplitude and modulation of the resonant energy are included to calculate the diffusion coefficient. Variation of loss cone size is not included when calculating the resultant electron precipitation using Equations (1) and (2). We calculate the ratio of the modeled precipitating flux with modulation of the equatorial loss cone size ("Modulated α_{LC} ") to the precipitating flux without ambient magnetic field modulation ("Smoothed") (Figure 6a), as well as the ratio of the precipitating flux with modulated $\langle D_{\alpha\alpha} \rangle_{LC}$ to the precipitating flux without modulation in $\langle D_{\alpha\alpha} \rangle_{LC}$ ("Smoothed") (Figure 6b). Rae et al. (2018) showed that the percent change in precipitating flux driven by the change in the equatorial loss cone depends significantly on electron pitch angle distribution close to the loss cone. In our case, it is shown that when there is only bounce loss cone modulation (Figure 6a), the precipitating flux increases (decreases) about 10% when magnetic field increases (decreases) by 10% for electrons with a broad range of energy (10 keV-300 keV in X-rays). However, for higher energy electrons, the precipitating flux shows an opposite trend, i.e., increases when α_{LC} decreases. This is caused by the competing effects of the loss cone size and averaged flux inside the loss cone. When loss cone size increases, it is harder for these higher energy electrons to form a filled loss cone under the

- equilibrium between pitch angle scattering and precipitation into the atmosphere, and the averaged flux
- inside the loss cone is smaller, leading to a lower value of total integrated precipitation. When there is
- only modulation in $\langle D_{\alpha\alpha} \rangle_{LC}$ (Figure 6b), the change in electron precipitation ratio also depends on their
- energies, increasing (decreasing) by up to about 20% for electrons with energy at 30 keV and about
- 360 50% for ~100 keV electrons when B_0 increases (decreases). We conclude that the magnetic field
- oscillation-driven modulation in $\langle D_{\alpha\alpha} \rangle_{LC}$, i.e., the resonance condition in precipitating rates, are larger
- than the effects of modulation in loss cone size by the ambient magnetic field oscillations.

5 Summary

363

386

393

- We present simultaneous multi-point observations of whistler-mode chorus waves and magnetospheric
- oscillations on a time scale of several to ~10s minutes, associated with concurrent energetic electron
- 366 precipitation observed through enhanced BARREL X-rays. Similar fluctuations on a time scale of
- several to ~10s minutes are observed in X-ray signatures and the compressional component of magnetic
- 368 field oscillations. The spatial scale of oscillations spans from \sim 9 to 12 h in MLT and from 5 to 11 in L
- 369 shell. Such magnetic field oscillations, which have been suggested to play a potential role in
- 370 precipitating energetic electrons by either wave amplitude, resonance energy or loss cone modulation,
- 371 show high correlations with enhancement in X-rays.
- We evaluate the relative role of breathing mode magnetic field oscillations in modulating the electron
- 373 precipitation through modulating the minimum resonant energy, the loss cone size and the chorus wave
- amplitude. We show that the modulation in energetic electron precipitation is dominated by the
- modulation of chorus wave amplitude. However, the effects of modulation in the resonance condition
- due to breathing mode magnetic field oscillations cannot be neglected. The ambient magnetic field
- oscillation could significantly modulate the electron precipitation observed through BARREL X-ray
- 378 (25–180 keV), increasing the precipitating flux by 50% when magnetic field increases by 5% by
- modulating the resonance condition. The modulation in the loss cone size has a much smaller effect on
- the electron precipitation modulation, increasing the precipitating flux (electrons observed through 10–
- 381 300 keV X-rays) by 10% when the ambient magnetic field increases by 5%.
- The study examines the relative role of different mechanisms that could be responsible for the electron
- precipitation modulated on ULF timescales or a longer period, which is important for understanding
- 384 the radiation belt electron loss. Nevertheless, multi-case or statistical studies are needed in the future
- 385 to systematically evaluate the relative roles of various mechanisms in different events and regions.

6 Conflict of Interest

- The authors declare that the research was conducted in the absence of any commercial or financial
- relationships that could be construed as a potential conflict of interest.

389 7 Author Contributions

- 390 MQ took the lead in writing the manuscript. WL, QM, XS, LW, RM and VA provided critical feedback
- and helped shape the research, analysis and manuscript. All authors contributed to manuscript revision,
- read, and approved the submitted version.

8 Funding

- 394 NASA grants of 80NSSC20K0698, 80NSSC19K0845, 80NSSC20K0196, 80NSSC21K1312, and the
- 395 NSF grant of AGS-1847818.

396 9 Acknowledgments

- 397 WL, QM, XS, and LC would like to acknowledge NASA grants of 80NSSC20K0698,
- 398 80NSSC19K0845, 80NSSC20K0196, 80NSSC21K1312, and the NSF grant of AGS-1847818. We
- acknowledge the BARREL team developers of IDL BDAS program for use of BARREL data. We
- 400 thank the NOAA National Geophysical Data Center for GOES data. We acknowledge V. Angelopoulos
- 401 for use of data from the THEMIS mission. We also acknowledge, specifically, C.W. Carlson and J.P.
- 402 McFadden for use of ESA data; K.H. Glassmeier, U. Auster, and W. Baumjohann for the use of FGM
- data provided under the lead of the Technical University of Braunschweig. The content of this
- manuscript has been presented in part at EGU22, the 24th EGU General Assembly. Citation: Qin, M.,
- 405 Li, W., Ma, O., Shen, X., and Shen, X.: Global magnetic field oscillations on the breathing-mode
- 406 timescale and their effects on energetic electron precipitation, EGU General Assembly 2022, Vienna,
- 407 Austria, 23–27 May 2022, EGU22-4057, https://doi.org/10.5194/egusphere-egu22-4057, 2022.
- 408

409

10 Data Availability Statement

- Data from the THEMIS mission are available from http://themis.ssl.berkeley.edu/data/themis/.
- 411 BARREL ephemeris, MSPC and FSPC data are available from
- 412 http://barreldata.ucsc.edu/data products/v05/12/.

413 11 Reference styles

- 414 Agapitov, O., Blum, L. W., Mozer, F. S., Bonnell, J. W., & Wygant, J. (2017). Chorus whistler wave
- source scales as determined from multipoint Van Allen Probe measurements. Geophysical Research
- 416 Letters, 44, 2634–2642. https://doi.org/10.1002/2017GL072701
- 417 Angelopoulos, V. (2008), The THEMIS mission, Space Sci. Rev., 141, 5–34, doi:10.1007/s11214-
- 418 008-9336-1.
- 419 Artemyev, A. V., Angelopoulos, V., & McTiernan, J. M. (2018). Near-Earth solar wind: Plasma
- characteristics from ARTEMIS measurements. Journal of Geophysical Research: Space Physics, 123,
- 421 9955–9962. https://doi-org.ezproxy.bu.edu/10.1029/2018JA025904.
- 422 Auster, H. U., et al. (2008), The THEMIS fluxgate magnetometer, Space Sci. Rev., 141, 235–264,
- 423 doi:10.1007/s11214-008-9365-9.
- Berger, M.J., and S.M. Seltzer, Bremsstrahlung in the atmosphere, Journal of Atmospheric and
- 425 Terrestrial Physics, Volume 34, Issue 1, 1972, Pages 85-108, ISSN 0021-9169,
- 426 https://doi.org/10.1016/0021-9169(72)90006-2.
- 427 Bonnell, J. W., F. S. Mozer, G. T. Delory, A. J. Hull, R. E. Ergun, C. M. Cully, V. Angelopoulos,
- and P. R. Harvey (2008). The Electric Field Instrument (EFI) for THEMIS, Space Sci.
- 429 Rev., 141, 303–341, doi:10.1007/s11214-008-9469-2.
- 430 Breneman, A. W., Halford, A., Millan, R., McCarthy, M., Fennell, J., Sample, J., et al. (2015).
- Global-scale coherence modulation of radiation-belt electron loss from plasmaspheric hiss. Nature,
- 432 523(7559), 193–195. https://doi.org/10.1038/nature14515
- Breneman, A. W., Halford, A. J., Millan, R. M., Woodger, L. A., Zhang, X.-J., Sandhu, J. K., et al.
- 434 (2020). Driving of Outer Belt Electron Loss by Solar Wind Dynamic Pressure Structures: Analysis of

- 435 Balloon and Satellite Data. Journal of Geophysical Research: Space Physics, 125(12).
- 436 https://doi.org/10.1029/2020ja028097
- 437 Brito, T., Woodger, L., Hudson, M., & Millan, R. (2012). Energetic radiation belt electron
- 438 precipitation showing ULF modulation. Geophysical Research Letters, 39(22).
- 439 https://doi.org/10.1029/2012gl053790
- Brito, T., Hudson, M., Kress, B., Paral, J., Halford, A., Millan, R., & Usanova, M. (2015). Simulation
- of ULF wave-modulated radiation belt electron precipitation during the 17 March 2013 storm.
- Journal of Geophysical Research: Space Physics, 120(5), 3444–3461.
- 443 https://doi.org/10.1002/2014ja020838
- Buchert, S. C., Fujii, R., & Glassmeier, K.-H. (1999). Ionospheric conductivity modulation in ULF
- pulsations. Journal of Geophysical Research: Space Physics (1978–2012), 104(A5), 10119–10133.
- 446 https://doi.org/10.1029/1998ja900180
- Capannolo, L., Li, W., Ma, Q., Chen, L., Shen, X.-C., Spence, H. E., et al. (2019a). Direct
- Observation of Subrelativistic Electron Precipitation Potentially Driven by EMIC Waves.
- 449 Geophysical Research Letters, 46(22), 12711–12721. https://doi.org/10.1029/2019gl084202
- 450 Capannolo, L., Li, W., Ma, Q., Shen, X.-C., Zhang, X.-J., Redmon, R. J., et al. (2019b). Energetic
- 451 Electron Precipitation: Multievent Analysis of Its Spatial Extent During EMIC Wave Activity.
- Journal of Geophysical Research: Space Physics, 124(4), 2466–2483.
- 453 https://doi.org/10.1029/2018ja026291.
- 454 Chen, L., R. M. Thorne, W. Li, J. Bortnik, D. Turner, and V. Angelopoulos (2012), Modulation of
- plasmaspheric hiss intensity by thermal plasma density structure, Geophys. Res. Lett., 39, L14103,
- 456 doi:10.1029/2012GL052308.
- Claudepierre, S. G., M. Wiltberger, S. R. Elkington, W. Lotko, and M. K. Hudson (2009).
- 458 Magnetospheric cavity modes driven by solar wind dynamic pressure fluctuations, Geophys. Res.
- 459 Lett., 36, L13101, doi:10.1029/2009GL039045.
- 460 Claudepierre, S., M. Hudson, W. Lotko, J. Lyon, and R. Denton (2010). Solar wind driving of
- magnetospheric ULF waves: Field line resonances driven by dynamic pressure fluctuations, J.
- 462 Geophys. Res., 115, A11202, doi:10.1029/2010JA015399
- 463 Clilverd, M. A., Duthie, R., Hardman, R., Hendry, A. T., Rodger, C. J., Raita, T., et al. (2015).
- Electron precipitation from EMIC waves: A case study from 31 May 2013. Journal of Geophysical
- 465 Research: Space Physics, 120(5), 3618–3631. https://doi.org/10.1002/2015ja021090
- Elkington, S. R., Hudson, M. K., and Chan, A. A. (2003), Resonant acceleration and diffusion of
- outer zone electrons in an asymmetric geomagnetic field, J. Geophys. Res., 108, 1116,
- 468 doi:10.1029/2001JA009202, A3.
- Grach, V. S., Artemyev, A. V., Demekhov, A. G., Zhang, X.-J., Bortnik, J., Angelopoulos, V., et al.
- 470 (2022). Relativistic electron precipitation by EMIC waves: Importance of nonlinear resonant effects.
- 471 Geophysical Research Letters, 49, e2022GL099994. https://doi. org/10.1029/2022GL099994
- Hendry, A. T., Rodger, C. J., & Clilverd, M. A. (2017). Evidence of sub-MeV EMIC-driven electron
- 473 precipitation. Geophysical Research Letters, 44(3), 1210–1218.
- 474 https://doi.org/10.1002/2016gl071807
- Halford, A., McGregor, S., Murphy, K., Millan, R., Hudson, M., Woodger, L., et al. (2015).
- 476 BARREL observations of an ICME-shock impact with the magnetosphere and the resultant radiation

- belt electron loss. Journal of Geophysical Research: Space Physics, 120(4), 2557–2570.
- 478 <u>https://doi.org/10.1002/2014ja020873</u>
- Hosokawa, K., Miyoshi, Y., Ozaki, M. et al. Multiple time-scale beats in aurora: precise
- orchestration via magnetospheric chorus waves. Sci Rep 10, 3380 (2020).
- 481 https://doi.org/10.1038/s41598-020-59642-8
- Heacock, R., & Hunsucker, R. (1977). A study of concurrent magnetic field and particle precipitation
- pulsations, 0.005 to 0.5 Hz, recorded near College, Alaska. Journal of Atmospheric and Terrestrial
- 484 Physics, 39(4), 487–501. https://doi.org/10.1016/0021-9169(77)90158-1.
- 485 Hsu, T., and R. L. McPherron (2007). A statistical study of the relation of Pi 2 and plasma flows in
- 486 the tail, J. Geophys. Res., 112, A05209, doi:10.1029/2006JA011782.
- Jaynes, A., Lessard, M., Takahashi, K., Ali, A., Malaspina, D., Michell, R., et al. (2015). Correlated
- 488 Pc4–5 ULF waves, whistler-mode chorus, and pulsating aurora observed by the Van Allen Probes
- and ground-based systems. Journal of Geophysical Research: Space Physics, 120(10), 8749–8761.
- 490 https://doi.org/10.1002/2015ja021380
- Kennel, C. F., & Petschek, H. E. (1966). Limit on stably trapped particle fluxes. Journal of
- 492 Geophysical Research, 71(1), 1–28. https://doi.org/10.1029/jz071i001p00001
- Kepko, L., Spence, H. E., and Singer, H. J. (2002), ULF waves in the solar wind as direct drivers of
- magnetospheric pulsations, Geophys. Res. Lett., 29(8), doi:10.1029/2001GL014405.
- Kepko, L., and H. E. Spence (2003). Observations of discrete, global magnetospheric oscillations
- directly driven by solar wind density variations, J. Geophys. Res., 108(A6), 1257,
- 497 doi:10.1029/2002JA009676
- Kepko, L., & Viall, N. M. (2019). The source, significance, and magnetospheric impact of periodic
- density structures within stream interaction regions. J. Geophys. Res.: Space Physics, 124, 7722–
- 500 7743. https://doi.org/10.1029/ 2019JA026962
- Li, W., Thorne, R. M., Bortnik, J., Nishimura, Y., and Angelopoulos, V. (2011a). Modulation of
- whistler mode chorus waves: 1. Role of compressional Pc4–5 pulsations, J. Geophys. Res., 116,
- 503 A06205, doi:10.1029/2010JA016312.
- Li W., Bortnik, J., Thorne, R. M., Nishimura, Y., Angelopoulos, V., and Chen,
- L. (2011b). Modulation of whistler mode chorus waves: 2. Role of density variations, J. Geophys.
- 506 Res., 116, A06206, doi:10.1029/2010JA016313.
- Li, W., Shen, X.-C., Ma, Q., Capannolo, L., Shi, R., Redmon, R. J., et al. (2019). Quantification of
- 508 Energetic Electron Precipitation Driven by Plume Whistler Mode Waves, Plasmaspheric Hiss, and
- 509 Exohiss. Geophysical Research Letters, 46(7), 3615–3624. https://doi.org/10.1029/2019gl082095
- 510 Li, Z., et al. (2014), Investigation of EMIC wave scattering as the cause for the BARREL 17 January
- 2013 relativistic electron precipitation event: A quantitative comparison of simulation with
- 512 observations, Geophys. Res. Lett., 41, 8722–8729, doi:10.1002/2014GL062273.
- Liu, X., Gu, W., Xia, Z., Chen, L., & Horne, R. B. (2021). Frequency-dependent modulation of
- whistler-mode waves by density irregularities during the recovery phase of a geomagnetic
- storm. Geophysical Research Letters, 48, e2021GL093095. https://doi.org/10.1029/2021GL093095
- Ma, Q., Connor, H. K., Zhang, X.-J., Li, W., Shen, X.-C., Gillespie, D., et al. (2020). Global survey
- of plasma sheet electron precipitation due to whistler mode chorus waves in Earth's magnetosphere.
- 518 Geophysical Research Letters, 47, e2020GL088798, doi:10.1029/2020GL088798.

- 519 Ma, Q., Li, W., Zhang, X. -J., Bortnik, J., Shen, X. -C., Connor, H. K., et al. (2021). Global survey of
- electron precipitation due to hiss waves in the Earth's plasmasphere and plumes. Journal of
- 521 Geophysical Research: Space Physics, 126, e2021JA029644, doi:10.1029/2021JA029644.
- Mathie, R. A., & Mann, I. R. (2000). A correlation between extended intervals of ULF wave power
- and storm-time geosynchronous relativistic electron flux enhancements. Geophysical Research
- 524 Letters, 27(20), 3261–3264. https://doi-org.ezproxy.bu.edu/10.1029/2000GL003822.
- Millan, R. M., and R. M. Thorne (2007). Review of radiation belt relativistic electron loss, J. Atmos.
- 526 Sol. Terr. Phys., 69, 362–377, doi:10.1016/j.jastp.2006.06.019.
- Millan, R. M., et al. (2013). The Balloon Array for RBSP Relativistic Electron Losses (BARREL),
- 528 Space Sci. Rev., 179(1-4), 503–530, doi:10.1007/s11214-013-9971-z.
- Motoba, T., Takahashi, K., Gjerloev, J., Ohtani, S., & Milling, D. (2013). The role of compressional
- Pc5 pulsations in modulating precipitation of energetic electrons. Journal of Geophysical Research:
- 531 Space Physics, 118(12), 7728–7739. https://doi.org/10.1002/2013ja018912.
- Ni, B., R. M. Thorne, Y. Y. Shprits, and J. Bortnik (2008). Resonant scattering of plasma sheet
- electrons by whistler-mode chorus: Contribution to diffuse auroral precipitation, Geophys. Res. Lett.,
- 534 35, L11106, doi:10.1029/2008GL034032.
- Ni, B., Bortnik, J., Thorne, R. M., Ma, Q., & Chen, L. (2013). Resonant scattering and resultant pitch
- angle evolution of relativistic electrons by plasmaspheric hiss. Journal of Geophysical Research:
- 537 Space Physics, 118, 7740–7751. https://doi.org/10.1002/2013JA019260
- Nishimura, Y., et al. (2010). Identifying the driver of pulsating aurora, Science, 330, 81–84.
- Nishimura, Y., et al. (2011), Multievent study of the correlation between pulsating aurora and whistler
- mode chorus emissions, J. Geophys. Res., 116, A11221, doi:10.1029/2011JA016876.
- Olson, J. V. (1999). Pi2 pulsations and substorm onsets: A review, J. Geophys. Res., 104, 17,499–
- 542 17,520, doi:10.1029/1999JA900086.
- Pedersen, A., et al. (2008), Electron density estimations derived from spacecraft potential
- 544 measurements on Cluster in tenuous plasma regions, J. Geophys. Res., 113, A07S33,
- 545 doi:10.1029/2007JA012636.
- Pu, Z.-Y., and M. G. Kivelson (1983). Kelvin-Helmholtz instability at the magnetopause: Solution
- for compressible plasmas, J. Geophys. Res., 88(A2), 841–852.
- Qin, M., Hudson, M., Millan, R., Woodger, L., & Shekhar, S. (2018). Statistical Investigation of the
- 549 Efficiency of EMIC Waves in Precipitating Relativistic Electrons. Journal of Geophysical Research:
- 550 Space Physics, 123(8), 6223–6230. https://doi.org/10.1029/2018ja025419
- Oin, M., Hudson, M., Li, Z., Millan, R., Shen, X., Shprits, Y., et al. (2019). Investigating Loss of
- Relativistic Electrons Associated With EMIC Waves at Low L Values on 22 June 2015. Journal of
- 553 Geophysical Research: Space Physics, 124(6), 4022–4036. https://doi.org/10.1029/2018ja025726
- Oin, M., Hudson, M., Millan, R., Woodger, L., & Shen, X. (2020). Statistical Dependence of EMIC
- Wave Scattering on Wave and Plasma Parameters. Journal of Geophysical Research: Space Physics,
- 556 125(4). https://doi.org/10.1029/2020ja027772
- Oin, M., Li, W., Ma, Q., Woodger, L., Millan, R., Shen, X.-C., & Capannolo, L. (2021). Multi-point
- observations of modulated whistler-mode waves and energetic electron precipitation. Journal of
- Geophysical Research: Space Physics, 126, e2021JA029505. https://doi-org/10.1029/2021JA029505

- Rae, I. J., Mann, I. R., Dent, Z. C., Milling, D. K., Donovan, E. F., & Spanswick, E. (2007). Multiple
- 561 field line resonances: Optical, magnetic and absorption signatures. *Planetary and Space Science*,
- 562 55(6), 701–713. https://doi.org/10.1016/j.pss.2006.02.009
- 563 Rae, J. I., Murphy, K. R., Watt, C. E., Halford, A. J., Mann, I. R., Ozeke, L. G., et al. (2018). The
- Role of Localized Compressional Ultra-low Frequency Waves in Energetic Electron Precipitation.
- Journal of Geophysical Research: Space Physics, 123(3), 1900–1914.
- 566 <u>https://doi.org/10.1002/2017ja024674.</u>
- Roux, A., O. Le Contel, C. Coillot, A. Bouabdellah, B. de la Porte, D. Alison, S. Ruocco, and M. C.
- Vassal (2008). The search coil magnetometer for THEMIS, Space Sci. Rev., 141, 265–275,
- 569 doi:10.1007/s11214-008-9455-8.
- 570 Shen, X., Q.-G. Zong, Q. Shi, A. Tian, W. Sun, Y. Wang, X. Zhou, S. Fu, M. Hartinger, and V.
- Angelopoulos (2015). Magnetospheric ULF waves with increasing amplitude related to solar wind
- dynamic pressure changes: The time history of events and macroscale interactions during substorms
- 573 (THEMIS) observations, J. Geophys. Res. Space Physics, 120, 7179–7190,
- 574 doi:10.1002/2014JA020913.
- 575 Shen, X. C., et al. (2017). Dayside magnetospheric ULF wave frequency modulated by a solar wind
- 576 dynamic pressure negative impulse, J. Geophys. Res. Space
- 577 Physics, 122, 1658–1669, doi:10.1002/2016JA023351.
- 578 Shen, X.-C., Li, W., Ma, Q., Agapitov, O., & Nishimura, Y. (2019). Statistical analysis of transverse
- size of lower band chorus waves using simultaneous multisatellite observations. *Geophysical*
- 580 Research Letters, 46, 5725–5734. https://doi.org/10.1029/2019GL083118
- Singer, H., Matheson, L., Grubb, R., Newman, A., & Bouwer, D. (1996). Monitoring space weather
- with the GOES magnetometers. In GOES-8 and beyond (Vol. 2812, pp. 299–308). Bellingham,
- Washington: International Society for Optics and Photonics. https://doi-
- 584 org.ezproxy.bu.edu/10.1117/12.254077
- 585 Spanswick, E., Donovan, E., & Baker, G. (2005). Pc5 modulation of high energy electron
- precipitation: particle interaction regions and scattering efficiency. Annales Geophysicae, 23(5),
- 587 1533–1542. https://doi.org/10.5194/angeo-23-1533-2005
- Summers, D., and R. M. Thorne (2003). Relativistic electron pitch-angle scattering by
- electromagnetic ion cyclotron waves during geomagnetic storms, J. Geophys. Res., 108(A4), 1143,
- 590 doi:10.1029/2002JA009489.
- 591 Summers, D., Ni, B., Meredith, N. P., Horne, R. B., Thorne, R. M., Moldwin, M. B., and Anderson,
- R. R. (2008). Electron scattering by whistler-mode ELF hiss in plasmaspheric plumes, J. Geophys.
- 593 Res., 113, A04219, doi:10.1029/2007JA012678.
- Thorne, R. M. (2010), Radiation belt dynamics: The importance of wave-particle
- 595 interactions, Geophys. Res. Lett., 37, L22107, doi:10.1029/2010GL044990.
- Tsyganenko (1989). A magnetospheric magnetic field model with a warped tail current sheet,
- 597 Planetary and Space Science, Volume 37, Issue 1, Pages 5-20, ISSN 0032-0633,
- 598 https://doi.org/10.1016/0032-0633(89)90066-4.
- Woodger, L. A., A. J. Halford, R. M. Millan, M. P. McCarthy, D. M. Smith, G. S. Bowers, J. G.
- Sample, B. R. Anderson, and X. Liang (2015). A summary of the BARREL campaigns: Technique
- for studying electron precipitation, J. Geophys. Res. Space Physics, 120, 4922–4935,
- 602 doi:10.1002/2014JA020874.

- Xia, Z., Chen, L., Dai, L., Claudepierre, S. G., Chan, A. A., Soto-Chavez, A. R., and Reeves, G.
- D. (2016), Modulation of chorus intensity by ULF waves deep in the inner magnetosphere, Geophys.
- 605 Res. Lett., 43, 9444–9452, doi:10.1002/2016GL070280.
- Yin, Z.-F., Zhou, X.-Z., Li, W., Shen, X.-C., Rankin, R., Liu, J., et al. (2023). Characteristics of
- 607 electron precipitation directly driven by poloidal ULF waves. Journal of Geophysical Research:
- 608 Space Physics, 128, e2022JA031163. https://doi.org/10.1029/2022JA031163
- Zhang, X.-J., Mourenas, D., Artemyev, A. V., Angelopoulos, V., & Sauvaud, J.-
- A. (2019). Precipitation of MeV and sub-MeV electrons due to combined effects of EMIC and ULF
- waves. Journal of Geophysical Research: Space Physics, 124, 7923–7935. https://doi-
- 612 org.ezproxy.bu.edu/10.1029/2019JA026566
- Zhang, X.-J., Mourenas, D., Shen, X.-C., Qin, M., Artemyev, A. V., Ma, Q., & Angelopoulos,
- V. (2021). Dependence of relativistic electron precipitation in the ionosphere on EMIC wave
- minimum resonant energy at the conjugate equator. Journal of Geophysical Research, 126(5),
- 616 e2021JA029193. https://doi-org.ezproxy.bu.edu/10.1029/2021JA029193.
- Zhou, C., Li, W., Thorne, R. M., Bortnik, J., Ma, Q., An, X., Zhang, X.-j., Angelopoulos, V., Ni,
- B., Gu, X., et al. (2015), Excitation of dayside chorus waves due to magnetic field line compression
- in response to interplanetary shocks, J. Geophys. Res. Space Physics, 120, 8327–8338,
- 620 doi:10.1002/2015JA021530.

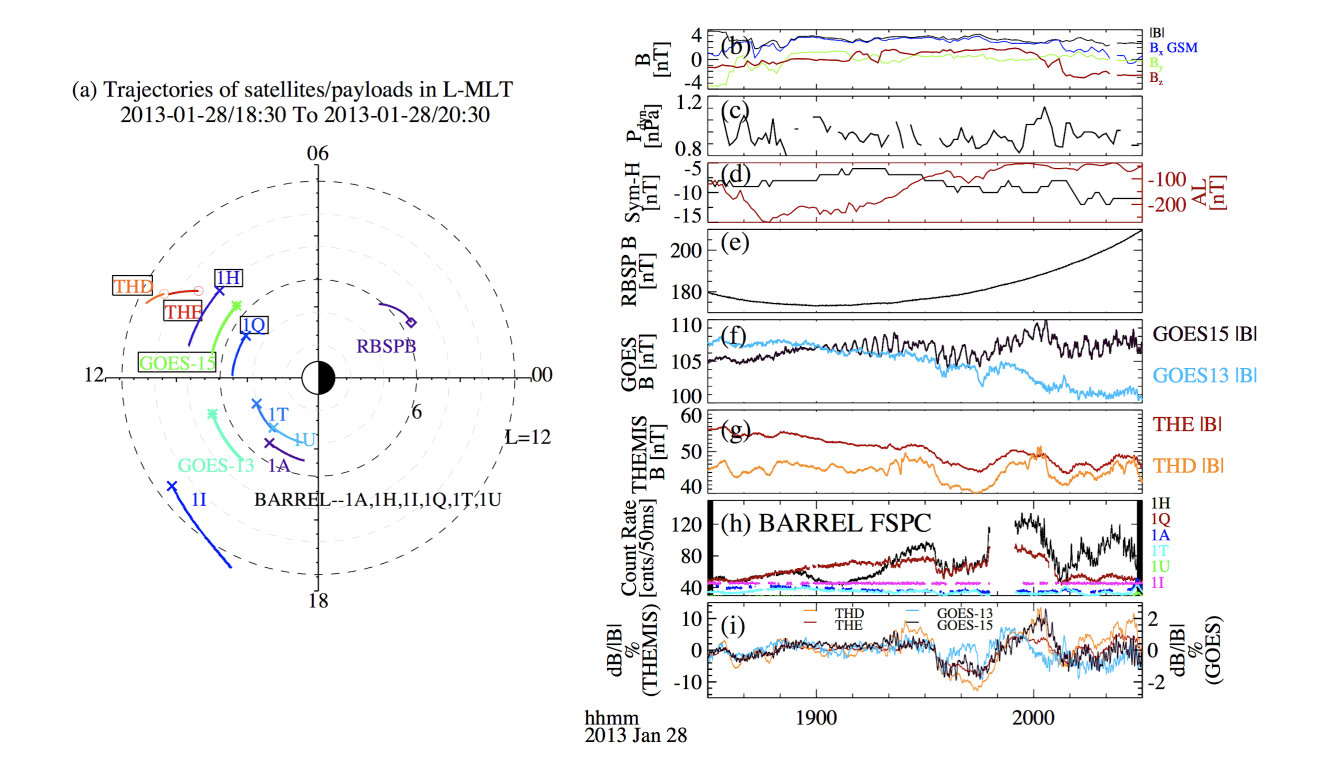


Figure 1. (a) Trajectories of BARREL payloads, RBSP, THEMIS and GOES satellites in the *L*-MLT map (IGRF model) during 18:30-20:30 UT. The circle, cross, asterisk, and diamond symbols indicate the start point of THEMIS, BARREL, RBSP and GOES. Satellites and payloads that observed the similar features of fluctuation are highlighted in the black box. The observations from the solar wind, magnetospheric spacecraft and BARREL payloads are shown in Panels (b-g). (b) Total magnetic field (black), Bx (blue), By (green), and Bz component (red) of the interplanetary magnetic field in GSM coordinates and (c) solar wind dynamic pressure obtained from OMNI database (a compilation of records made on ACE, WIND, and IMP-8 spacecraft that were time-shifted to the Earth's bow shock subsolar point); (d) Sym-H (black) and AL indices (red) showing a substorm onset at ∼18:30 UT; (e) Total magnetic field measured by RBSP-B; (f) Total magnetic field strength measured by GOES-13 (cyan) and 15 (black); (g) Total magnetic field measured by THEMIS D (orange) and E (red); (h) 25-180 keV X-ray count rate (smoothed over 0.5 s) measured by BARREL 1A (blue), 1H (black), 1I (magenta), 1Q (red), 1T (cyan) and 1U (green); (i) Percent variation (over 60 min smoothed background) of the magnetic field observed by THEMIS-D (orange), THEMIS-E (red), GOES-13 (cyan) and GOES-15 (black) relative to their 60 min smoothed data.

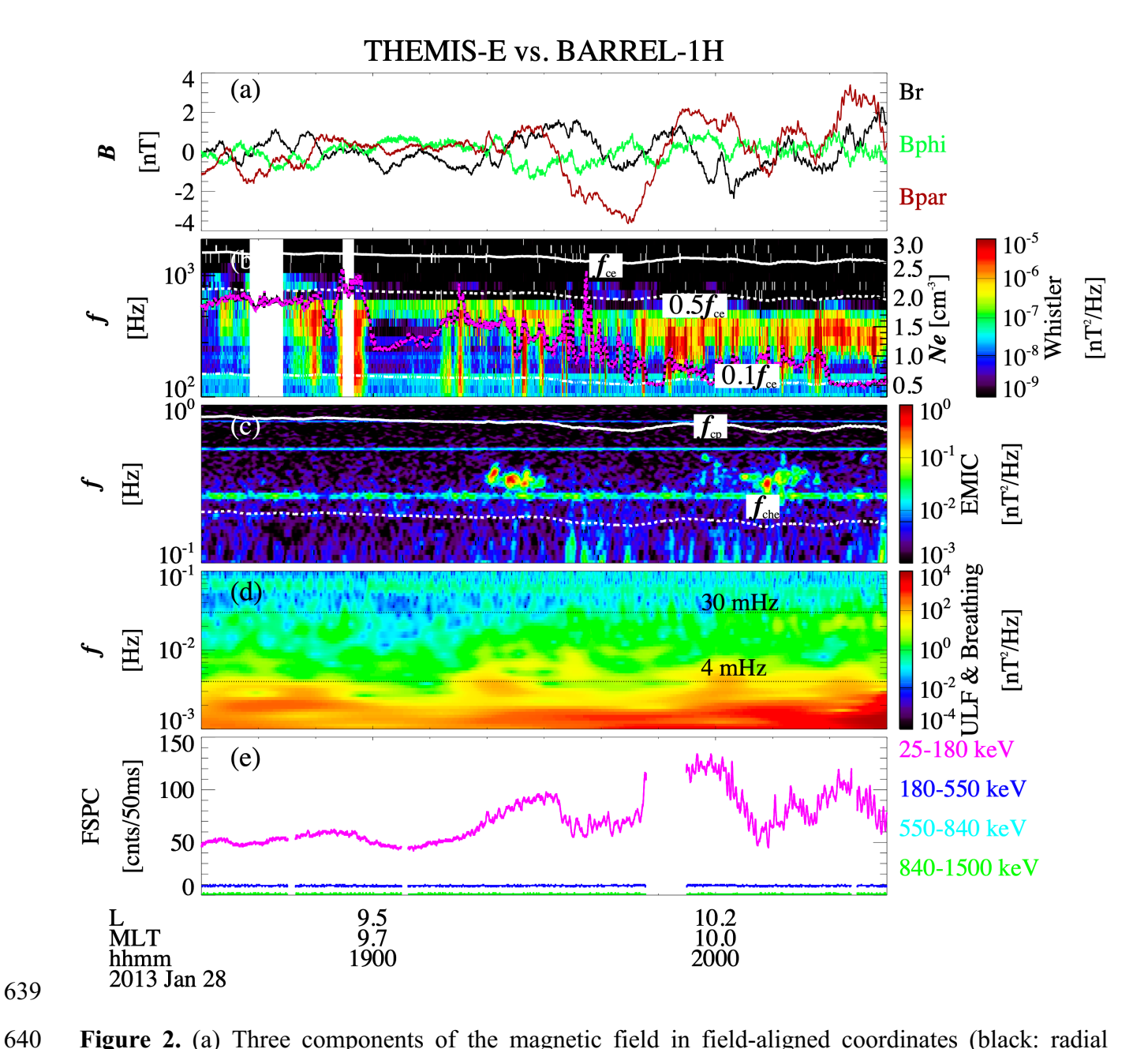


Figure 2. (a) Three components of the magnetic field in field-aligned coordinates (black: radial component, green: azimuthal component, red: compressional component) detrended over 60 min. (b) Magnetic spectral density observed by the Search Coil Magnetometer (SCM) onboard THEMIS-E. The white lines in panel (b) represent the electron cyclotron frequency (f_{ce}), 0.5 f_{ce} and 0.1 f_{ce} from top to bottom. The superimposed magenta line is the total electron density obtained from the spacecraft potential. (c) Magnetic spectral density calculated from the fluxgate magnetometer (FGM) onboard THEMIS-E. The white lines in panel (c) indicate proton, helium, and oxygen cyclotron frequencies. (d) Wavelet analysis of the magnetometer measurements, where the 4 mHz and 30 mHz frequencies are shown as the two black dotted lines. (e) BARREL 1H fast spectrum X-rays at energies of 25–180 (pink), 180-550 (blue), 550-840 (cyan), and 840-1500 keV (green).

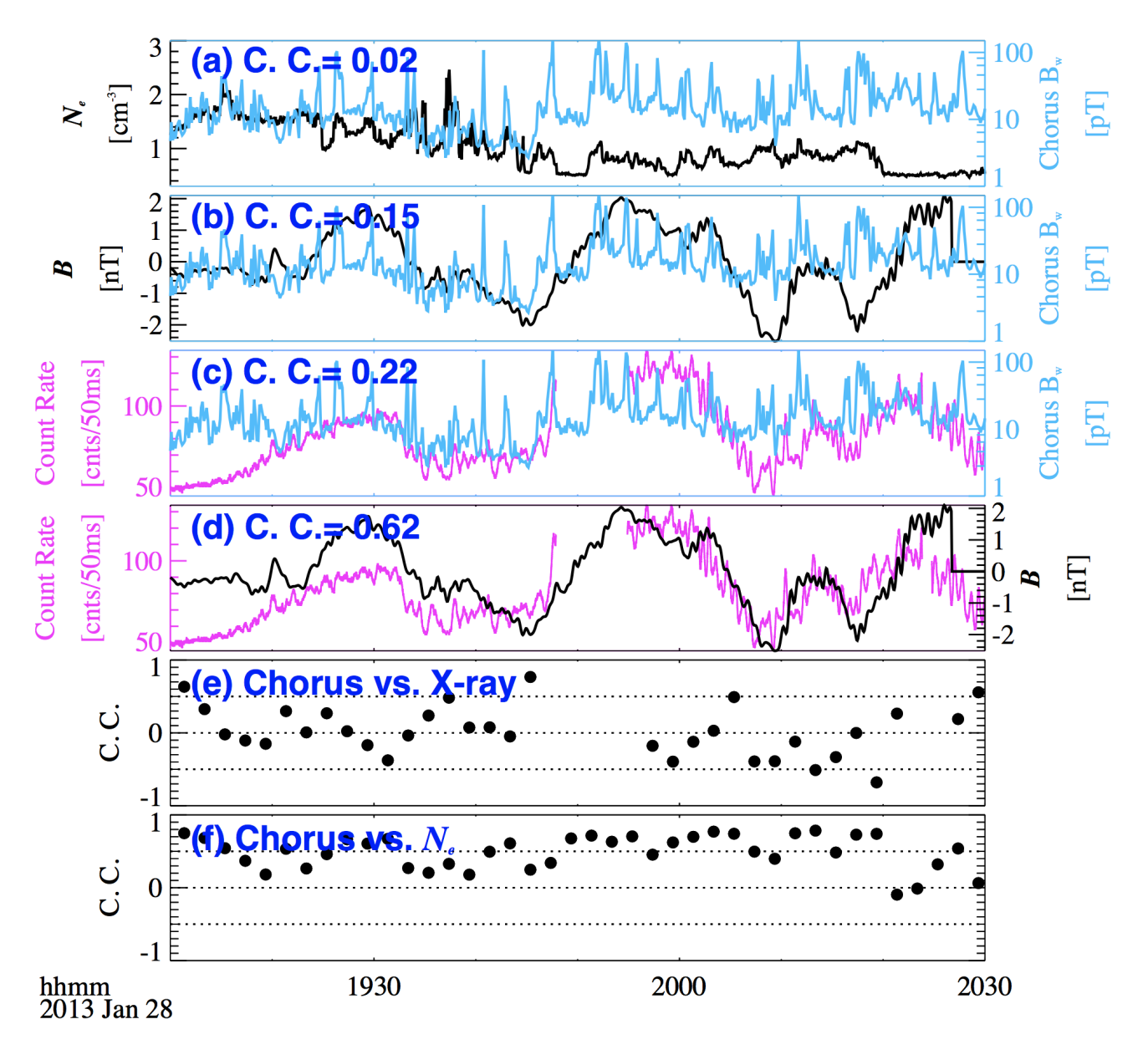


Figure 3. (a) Total electron density (black) obtained from spacecraft potential and chorus wave amplitude (blue) observed by THEMIS-E. (b) Ambient magnetic field fluctuations (0.6-30 mHz, black) and chorus wave amplitude (blue) observed by THEMIS-E with the time resolution of 4 s and 8 s, respectively. (c) Fast spectrum X-ray count rate (25-180 keV) from BARREL smoothed over 0.5 s (magenta) and chorus wave amplitude (blue). (d) Fast spectrum X-ray count rate (25-180 keV) from BARREL smoothed over 0.5 s (magenta) and ambient magnetic field fluctuations (0.6-30 mHz, black). Correlation coefficient between (e) chorus wave amplitude and X-ray count rate and (f) chorus wave amplitude and electron density.

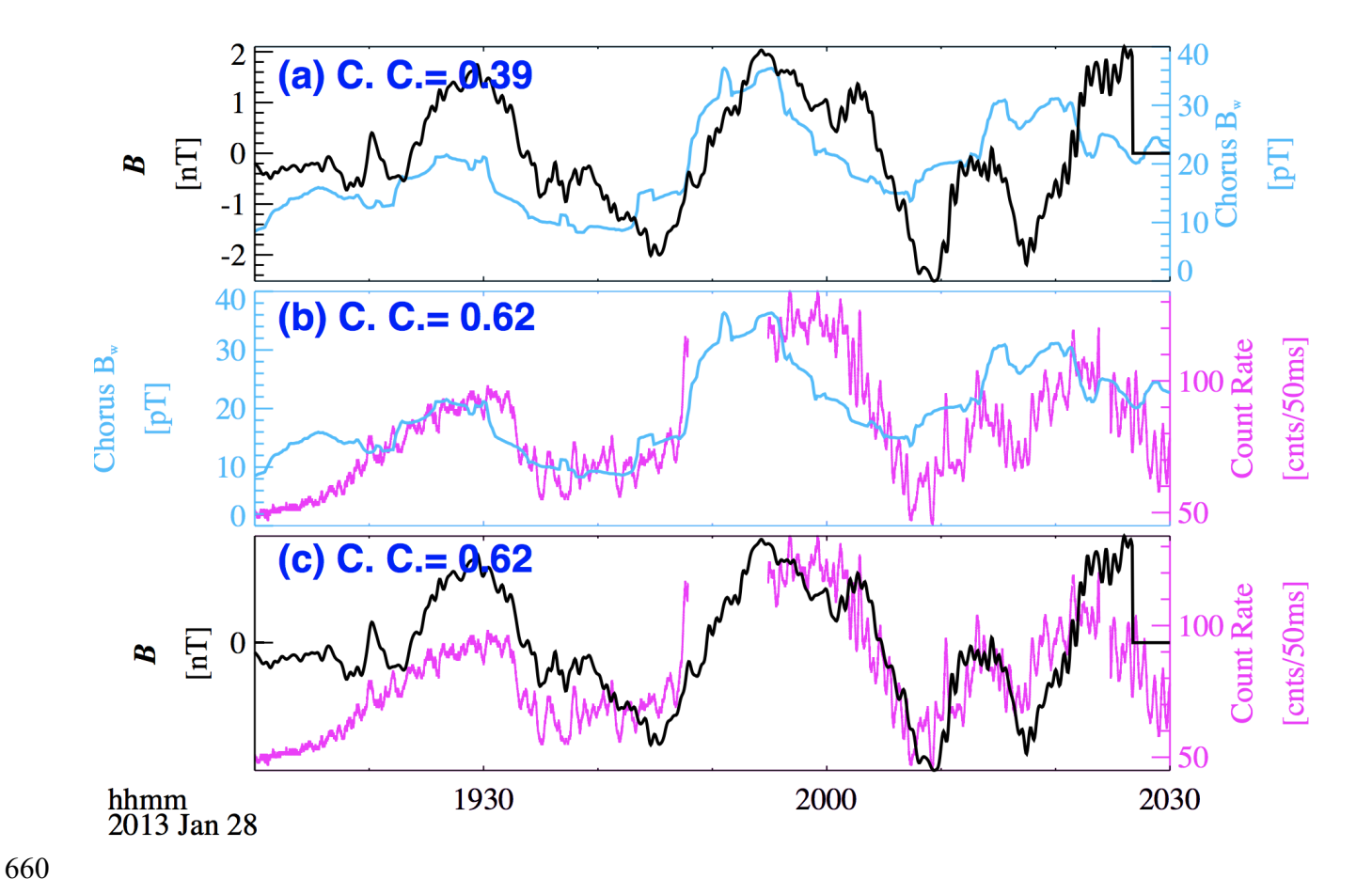


Figure 4. (a) Ambient magnetic field fluctuations (0.6-30 mHz, black) and chorus wave amplitude smoothed over 8 min (blue) observed by THEMIS-E with the time resolution of 4 s and 8 s, respectively. (b) Fast spectrum X-ray count rate (25-180 keV) from BARREL smoothed over 0.5 s (magenta) and chorus wave amplitude smoothed over 8 min (blue). (c) Fast spectrum X-ray count rate (25-180 keV) from BARREL smoothed over 0.5 s (magenta) and ambient magnetic field fluctuations (0.6-30 mHz, black).

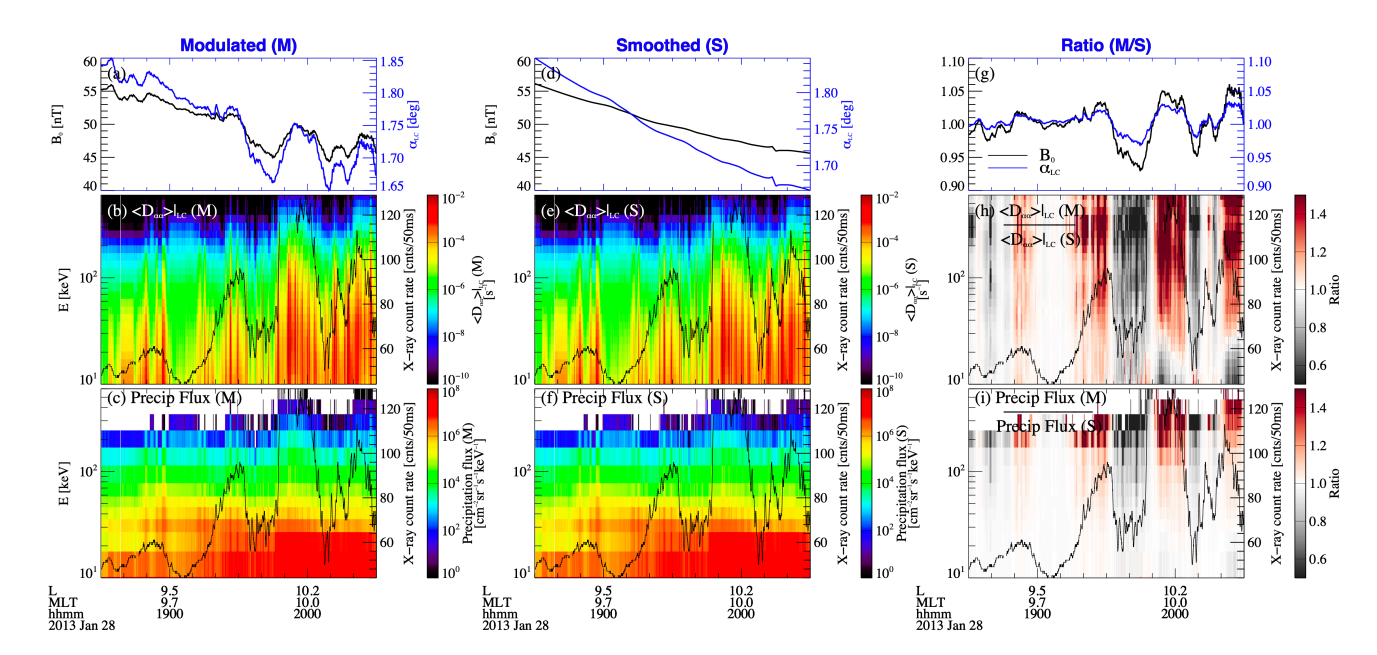


Figure 5. Analysis of electron precipitation due to chorus waves when the quasi-static breathing mode magnetic field modulation is considered (a-c) and excluded (d-f). (a) Measured ambient magnetic field strength and the corresponding bounce loss cone size calculated from the IGRF model; (b) Bounce-averaged pitch angle diffusion coefficients at the loss cone as a function of time and electron energy; (c) Model calculated electron precipitation at the equilibrium state from the quasi-linear theory as a function of time and electron energy. (d-e) Same format as panels (a-c) but with the quasi-static breathing mode turned off (Smoothed). Right panels (g-i) show the ratio between the left panels and the middle panels. The superimposed black lines in the bottom two rows represent fast spectrum X-ray count rate (25-180 keV) observed by BARREL.

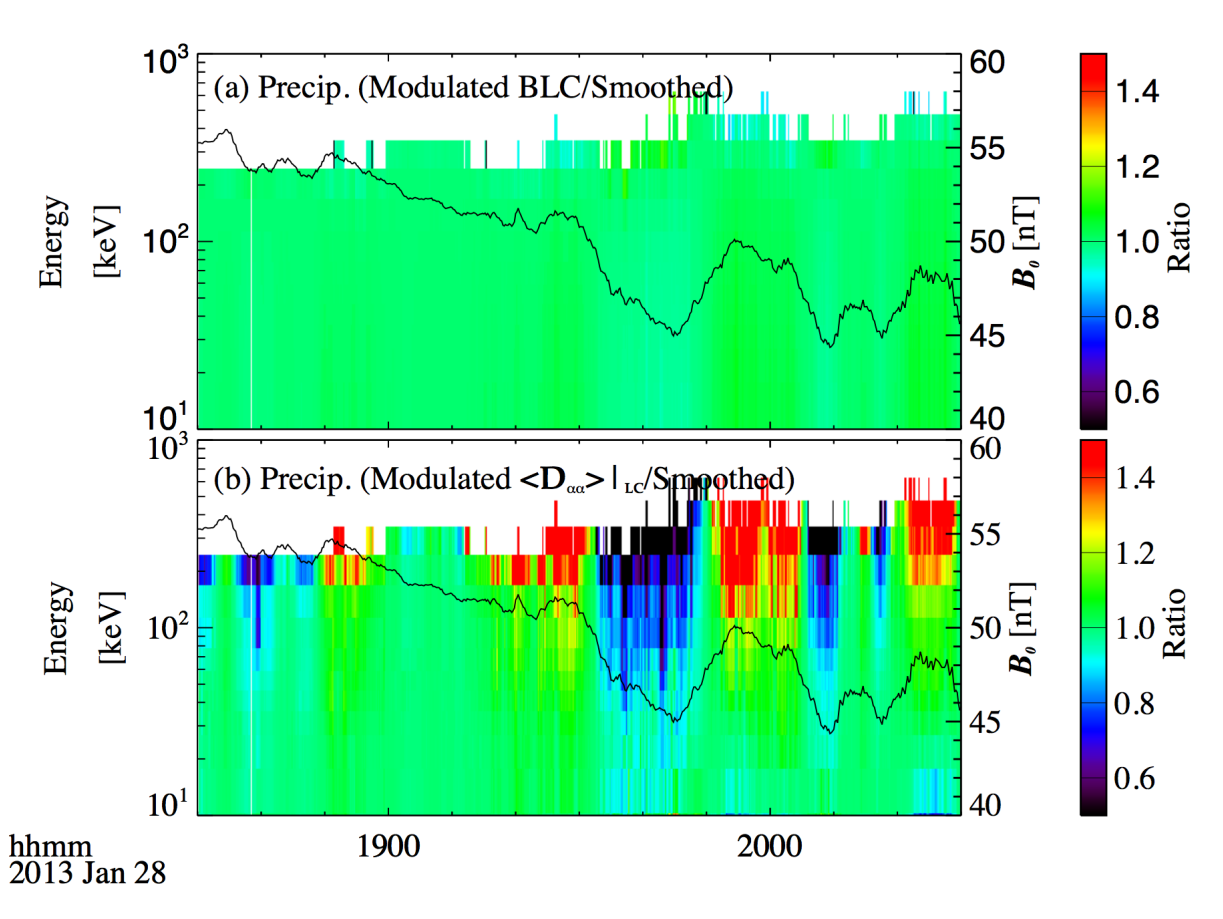


Figure 6. (a) Ratio of the calculated precipitating electron flux inside the loss cone with quasi-static breathing mode modulation of the equatorial loss cone size (Modulated BLC) to the precipitating flux without quasi-static breathing mode modulation (Smoothed). (b) Ratio of the calculated precipitating electron flux inside the loss cone with quasi-static breathing mode modulation of $\langle D_{\alpha\alpha} \rangle_{LC}$ to the precipitating flux without quasi-static breathing mode modulation (Smoothed).